RSC Advances

PAPER

View Article Online
View Journal | View Issue

Published on 01 March 2016. Downloaded by UNIVERSITY OF CINCINNATI on 23/09/2016 02:17:08.

Cite this: *RSC Adv.*, 2016, **6**, 25531

Enhanced mechanical properties of PLA/PLAE blends *via* well-dispersed and compatilized nanostructures in the matrix

Shenyang Cai,[a] Chao Zeng,[a] Naiwen Zhang,[b] Jianbo Li,[a] Markus Meyer,[c] Rainer H. Fink,[c] Donglu Shi[de] and Jie Ren*[abc]

Received 16th January 2016
Accepted 29th February 2016

DOI: 10.1039/c6ra01367h

www.rsc.org/advances

Polylactide (PLA) was toughened by a PLA-based thermoplastic elastomer (PLAE). PLAE was prepared by chain extension of PLA copolymer derived from polylactic acid (PLA) and poly(tetramethylene ether glycol) (PTMEG) *via* melt polycondensation. The tensile strength of the toughened-PLA (PLAE30) reached 70 MPa, while the elongation at break was found to be above 140% compared to its plain PLA counterpart. The relationship between the phase morphology of the blends and their mechanical behavior was investigated with atomic force microscopy (AFM), scanning electron microscopy (SEM), and scanning transmission X-ray microscopy (STXM). It was found that the well-dispersed nanoscale structures in the matrix of PLA/PLAE blends are mainly responsible for the significantly enhanced mechanical properties. Also discussed are the detailed microstructural development in PLAE and the toughening mechanism.

1. Introduction

Among several major commercial biodegradable polymers, polylactic acid (PLA) continues to increase its market share for its renewability, competitive cost, superb mechanical strength, and transparency.[1] However, one of its drawbacks: brittleness, still remains the main concern in industrial applications. The flexibility of PLA can be improved by copolymerization.[2] A number of investigations have been focused on blending of PLA with various polymers, for example, poly(ethylene glycol), poly(ε-caprolactone), poly(hydroxy butyrate), poly(hexamethylene succinate).[3,4] Among these modifications, melt blending is the most economic approach to improve its toughness.

The properties of the blend depend on the phase structure of each component as well as the interfaces between the domains. In blends, the phase structure and the mechanical properties are controlled by the weight ratio of the two components and dominated by the properties of the major phase.[5,6]

Co-polyesters with lower melting points are more suited for blending with PLA. The viscosity ratio (ratio of melt viscosity of PLA to that of other polymer) at the processing temperature should be kept between 0.1 and 10 for optimum dispersion. Poor interfacial adhesion will result in phase separation leading to embrittlement, a condition that is sensitively controlled by processing. Additionally, for some polymers, biodegradablility can be compromised by blending with PLA.[7,8]

Thermoplastic polyurethane (TPU) elastomer is an ideal candidate for medical devices owing to its flexibility, abrasion resistance, biocompatibility, and biological stability. TPU consists of both soft and hard segments with their ratios regulated for optimum mechanical properties. TPU can also be structurally tailored to having different hydrophilic/hydrophobic segments with good flexibilities compared to the methylene chains.[9–11] PLA in TPU may serve as a hard segment due to its high modulus, an effective way to reduce the brittleness of the composite.[12–15]

In this study, a polycondensation method[16] was utilized in the synthesis of PLA copolymer in which PTMEG macrodiol and lactic acid were used. These components reacted with HDI and butanediol (BDO)[17–19] to obtain a PLA-based thermoplastic elastomer (PLAE). The present study is an alternative approach to the previously reported works on the poly(lactic acid)-*block*-polycarbonate diol-[20–22] and polylactide-*block*-poly(butylene adipate) diol-[23–25] based thermoplastic elastomers. In this study, the PLA-based thermoplastic elastomer was blended with PLA to improve both thermal and mechanical properties. The operating mechanism is identified on the toughening of the PLA/PLAE blends.

[a]*Institute of Nano- and Bio-polymeric Materials, Key Laboratory of Advanced Civil Engineering Materials of Ministry of Education, School of Material Science and Engineering, Tongji University, Shanghai 201804, China. E-mail: renjie6598@163.com*

[b]*Shanghai Tong-jie-liang Biomaterials Co., Ltd, Shanghai 200438, China*

[c]*Physikalische Chemie II, Friedrich-Alexander Universität Erlangen-Nürnberg (FAU), Egerlandstrasse 3, 91058, Erlangen, Germany*

[d]*Shanghai East Hospital, The Institute for Biomedical Engineering and Nano Science, Tongji University School of Medicine, 150 Jimo Road, Shanghai 200120, China*

[e]*The Materials Science and Engineering Program, Department of Mechanical and Materials Engineering, College of Engineering & Applied Science, University of Cincinnati, Cincinnati, OH 45221-0012, USA*

Published on 01 March 2016. Downloaded by UNIVERSITY OF CINCINNATI on 23/09/2016 02:17:08.

2. Experimental section

2.1. Materials

PLA (grade 2002D) was manufactured by Natureworks, Inc. (Burgess, Virginia). L-Lactic acid (88 wt%) was purchased from Purac, Holland. Poly(tetramethylene ether glycol) (M_n = 2000 g mol^{-1}) was dried at 50 °C under high vacuum (0.1 Torr) for 12 hours before use. 1,6-Hexamethylene diisocyanate (HDI) and 1,4-butanediol (BDO) were purchased from Aldrich (Milwaukee). Chloroform and alcohol (99%) were purchased from Sinopharm Chemical Reagent Co., Ltd. (Shanghai, China). Other reagents were used as received.

2.2. Synthesis of PLA–PTMEG prepolymer (PLAG)

L-Lactic acid was purified by distillation under reduced pressure. 0.1 wt% $SnCl_2$ + TSA was used as a catalyst. The reaction was carried out under reduced pressure of 1000 Pa with mechanical stirring (rotational speed 140 rpm). The temperature increased at the rate of 10 °C h^{-1} from 80 °C to 165 °C. 25 wt% PTMEG was then added to the polymerization system (rotational speed increased to 160 rpm) under reduced pressure of 60 Pa. The temperature was maintained at 165 °C for 6 h.

2.3. Synthesis of PLA-based thermoplastic elastomer (PLAE)

PLA-glycol (PLAG) of 60 g obtained *via* polycondensation was added into a Haake Rheomix 600 with stable nitrogen stream while being mechanically stirred. The temperature was maintained at 170 °C. Subsequently, HDI and BDO (molar ratio = 3 : 2, total 16.7 wt% of PLAG) were added slowly to the mixture in 1 min. The reaction scheme is shown in Scheme 1. The resulting products (PLAG and PLAE) were purified by dissolution in chloroform and precipitating in excessive methanol. The purified products were dried to constant weight in a vacuum oven at room temperature for further experiments.

2.4. Preparation of PLA/PLAE blends

Melt blending was performed at a temperature of 165 °C in an extruder and a screw speed of 80 rpm in a Haake Rheomix 600 for 3 min. The samples are denoted by the weight% content of PLAE (Table 1). The polymer blends were dried in a vacuum oven for 24 hours at room temperature and stored in a desiccator for further characterization.

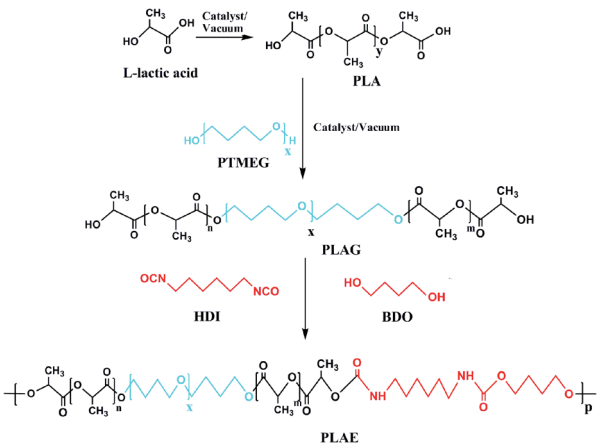

Scheme 1 Synthesis route of the PLA-based thermoplastic elastomer.

2.5. Polymer characterization

The average molecular weight and its distribution were determined by gas-phase chromatography (GPC) using a Waters 150C instrument coupled with a Waters differential refractometer. The polymer samples were dissolved in chloroform ($CHCl_3$; analytical grade) at a concentration of 1–2 mg mL^{-1}. The internal and column temperatures were kept constant at 35 °C. The molecular weights were calculated against polystyrene standards.

The copolymerization ratio and molecular structure of PLAE were determined by ^{1}H NMR spectroscopy (JEOL ECP-500). All spectra were obtained at room temperature from 15% (w/v) $CDCl_3$ solutions. Fourier-transform infra-red (FTIR) spectra were recorded with an EQUINOX 55 spectrometer using the compression molded film samples in the range 400–4000 cm^{-1}.

2.6. Mechanical properties

The mechanical properties were characterized using an Instron with the dog-bone-shaped specimens (4 mm × 50 mm × 2 mm) which were prepared by a HAAKE MiniJet piston injection molding system. The cross head speed was set at 20 mm min^{-1}. Tests were performed at room temperature. A minimum of seven specimens blend composition was tested. The tensile strength for all samples was obtained at the maximum stress of the stress–strain curves before rupture. Each experiment was repeated more than six times and the average test results were calculated for reproducibility of the data.

Dynamic mechanical properties (DMA) of the blends were measured with the DMA Q800 (TA Instruments) in a single-cantilever mode with an oscillating frequency of 1 Hz. The temperature was swept from 10 °C to 120 °C at 3 °C min^{-1}. The oscillation amplitude was 5.0 μm.

2.7. Differential scanning calorimeter (DSC)

For calorimetry the samples were sealed in Al-crucible pans and investigated by using a STA 449C differential scanning calorimeter (DSC). The samples were subjected to two consecutive DSC runs: at first, they were heated up to 180 °C, maintained for

Table 1 Labels of samples

Samples	PLAE	PLAE80	PLAE70	PLAE60	PLAE50
PLAE content/wt%	100	80	70	60	50
PLA content/wt%	0	20	30	40	50

Samples	PLAE40	PLAE30	PLAE20	PLAE10	PLA
PLAE content/wt%	40	30	20	10	0
PLA content/wt%	60	70	80	90	100

This journal is © The Royal Society of Chemistry 2016

Published on 01 March 2016. Downloaded by UNIVERSITY OF CINCINNATI on 23/09/2016 02:17:08.

2 min to eliminate the heat history, and then cooled down to −90 °C. Finally, they were heated up to 180 °C. All runs were conducted at a rate of 10 °C min^{-1} under nitrogen atmosphere. The degree of crystallinity (X_c) of the PLA component was determined using the following equation.

$$X_c = [(\Delta H_m - \Delta H_c)/w_f \Delta H_m^\circ] \times 100\%$$

where ΔH_m and ΔH_c are the enthalpies of melting and cold crystallization during the first heating cycle, respectively; ΔH_m° is the melting enthalpy assuming 100% crystalline PLA (93.7 J g^{-1}),[1] and w_f is the weight fraction of PLA in the blend.

2.8. Blend morphology characterization

The fractured surface morphology of the specimens was investigated by scanning electron microscopy (SEM) using a Hitachi S-2360N. All samples were gold coated prior to investigation. The SEM images were collected at an accelerating voltage of 10 kV. To investigate the blend morphology by atomic-force microscopy (AFM) the samples were cut into ultrathin sections of 70 nm thickness at room temperature with a diamond knife using a LeicaEMUC6 ultra-microtome. AFM (SPA-300HV) micrographs were acquired in tapping mode. STXM studies of PLAE and PLA/PLAE blends were conducted at the PolLux beamline at the Swiss Light Source (SLS), Paul Scherrer Institut, Switzerland.[26–30] The samples were microtomed into ultrathin sections of 70–200 nm thickness at room temperature and transferred to commercial TEM grids. The near-edge X-ray absorption fine structure (NEXAFS) contrast at the carbon/oxygen K-edge (photon energy of approximately 290/533 eV) provided strong chemical sensitivity and selectivity in organic materials. 2D composition maps were derived from STXM micrographs recorded at the major resonances of the respective components (288.1 eV/289.9 eV, and 532.5 eV/535.6 eV) or from image stacks.

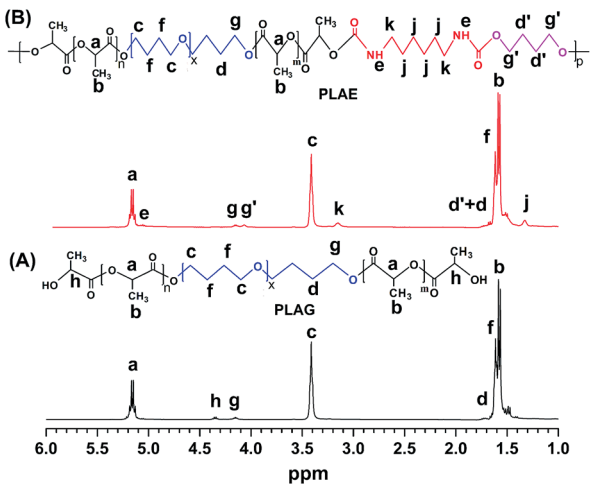

Fig. 1 ^{1}H NMR spectra of PLAE (top) and PLAG (bottom).

3. Results and discussion

3.1. Synthesis of the PLAG and PLAE

The intensity of methine proton in Fig. 1 can be used to calculate the number-average molecular weight ($M_{n,PLAG}$) of PLAG and the mass ratio according to the following equations:

$$M_{n,PLAG} = [2(I_a + I_k)/I_k + (I_c + I_g)/2I_k] \times 72 + 18$$

Mass ratio of monomer units of PLA:

$$\text{Monomer units of PTMEG} = 4(I_a + I_h)/(I_c + I_g)$$

where I_a, I_c, I_g, I_h represent the peak intensities of a, c, g and h respectively. 72 is the molar mass of a PLA repeat unit as well as that of PTMEG. 18 is the total molar mass of the remaining molecule. According to the ^{1}H NMR spectra and GPC results, the M_ns of PLAG and PLAE are listed in Table 2:

FTIR was utilized to analyse the interaction at the PLA and PLAE interfaces of the binary blends. Fig. 2 shows scale-expanded infrared spectra recorded at room temperature for blends with various PLAE contents. In the carbonyl groups stretching region (Fig. 2a), the absorption peaks at 1754 cm^{-1} observed in all blends are attributed to the stretching vibration of free carbonyl groups in PLA and PLAE. PLAE also exhibits a weak shoulder peak at 1718 cm^{-1} which is attributed to the H-bonding carbonyl groups. Another shoulder peak appearing at 1688 cm^{-1} indicates the formation of amide or urea dendritic structure in PLAE.[31,32] The band at 2200 cm^{-1} related to NCO is hardly observed, which is not shown in Fig. 2. The absorption peaks at 1718 cm^{-1} and 1688 cm^{-1} are also not observed in the binary blends with higher PLA content, *i.e.*, from PLAE50 to PLAE10.

The H-bonding involves carbonyl groups in PLA, which is often regarded as the H-bonding acceptor. Together with the NH groups in PLAE and OH groups in PLA, the carbonyl group is usually regarded as the H-bonding donor. The NH groups in PLAE and OH groups in PLA provide a favorable condition for the formation of H-bonding. The formation of the hydrogen bonding (intermolecular and/or intramolecular) influences the vibration of N–H band.[33,34] The ester carbonyl groups in PLA and PLAE simultaneously form the hydrogen bond with NH groups in the hard segments of PLAE (HDI and BDO section) and increase the compatibility between the PLA and PLAE segments, which results in the shift of the average position of the imide carbonyl's band from 3400 cm^{-1} to 3320 cm^{-1}, a lower wave number in FTIR spectra (Fig. 2b). The absorption peaks at

Table 2 ^{1}H NMR and GPC data of PLAG and PLAE

Sample	M_n[a]	M_n[b]	M_w[b]	PDI[b]	$[\eta]$ (dL g^{-1})	Mass ratio[a,c]
PLAG	4770	6680	12 430	1.86	0.193	0.87
PLAE	—	21 950	57 960	2.64	1.040	0.96

[a] Measured with relative integration obtained *via* ^{1}H NMR. [b] Data of M_n was obtained by GPC. [c] Mass ratio = n_{PLA} : n_{PTMEG}.

Published on 01 March 2016. Downloaded by UNIVERSITY OF CINCINNATI on 23/09/2016 02:17:08.

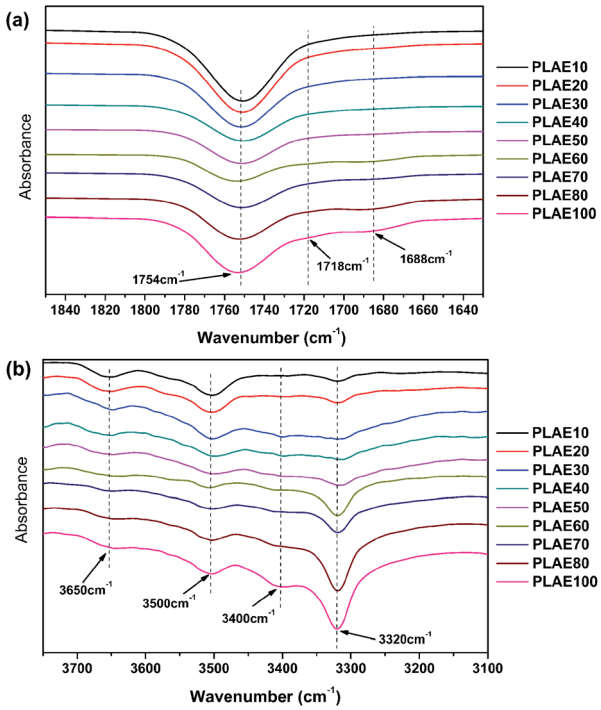

Fig. 2 FTIR absorption spectra for PLA/PLAE blends with various PLAE contents in the range of (a) 1630–1850 cm^{-1} and (b) the range of 3100–3750 cm^{-1}.

3500 cm^{-1} and 3650 cm^{-1} represent the vibration of hydroxyl groups in all blends. It is also noted that the NH groups at 3320 cm^{-1} are apparently stronger than that of the free NH groups at 3400 cm^{-1}.

However, the absorption peaks of PLAE at 1754 cm^{-1} related to free carbonyl groups are stronger than that of the H-bonding carbonyl groups, attributable to the difference in the number of carbonyl and NH groups. Most of the NH groups form hydrogen bonds with carbonyl groups, but most of the carbonyl groups remain without the H-bonding status. This can lead to phase separation between the PLA and PTMEG domains. Chen *et al.* reported two absorption characteristics of the proton acceptor, and concluded that the H-bonding disruption occurs either at domain interfaces or phase mixing of the hard and soft segments.[35]

3.2. Thermal properties, miscibility and crystallinity of PLA/PLAE blends

The thermal properties, miscibility and crystallinity of the PLA/PLAE blends were characterized by differential scanning calorimetry (DSC). Fig. 3a–c shows the DSC curves of blends with various constituent compositions. The melting temperature (T_m), crystallization temperature (T_c), crystallization heat (ΔH_c), and fusion heat (ΔH_m) were obtained from the first heating curve, as the PLA in the molded samples was in the original crystalline state. The crystallinity of the samples was determined by the ratio of their enthalpy of fusion to that of the PLA crystal ΔH_m° (we used a value of 93.7 J g^{-1}).[1] Table 3 summarizes

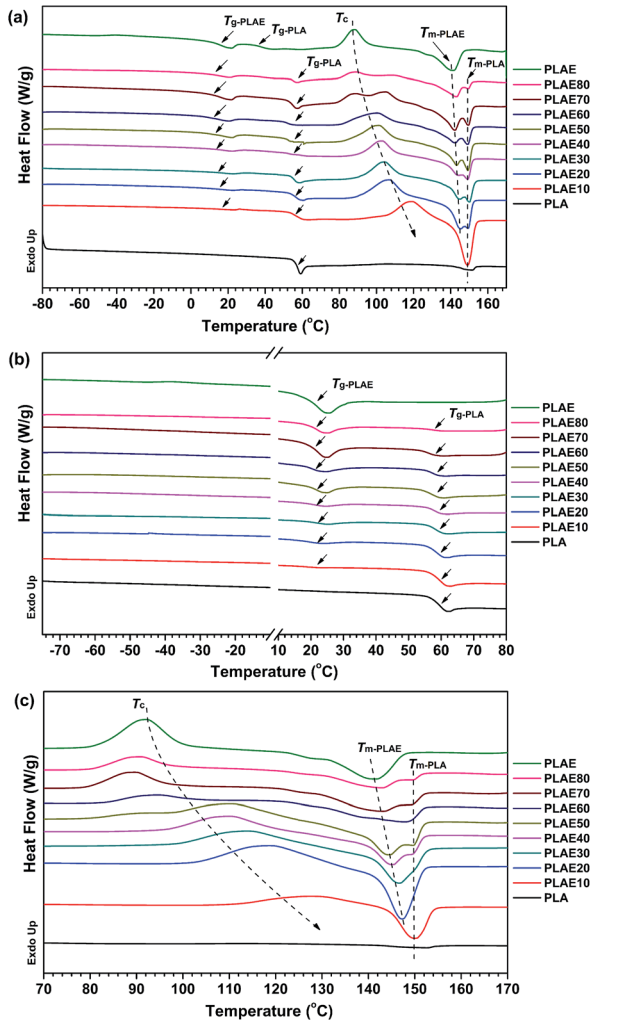

Fig. 3 DSC thermograms of (a) the first scan of PLA/PLAE blends, (b) the second scan of PLA/PLAE blends in the regime from −75 °C to 80 °C, and (c) the second scan of PLA/PLAE blends in the high-temperature range from 70–170 °C.

the results obtained from the heating runs for all investigated blends.

Fig. 3a clearly shows that PLAE has two glass transition temperatures (T_g) at 17.05 °C ($T_{g\text{-PLAE}}$), and 37.68 °C ($T_{g\text{-PLA}}$) in the first run. However, $T_{g\text{-PLAE}}$ and $T_{g\text{-PLA}}$ of PLAE in the second run (Fig. 3c) are hardly observed. This finding is attributed to the chain reorganization of PLAE during the DSC test, and to the fine dispersion of the short uncrystallized HDI/BDO hard segment in the PLA and PLAE domains.[36] The PLAE polyurethane in this study shows a T_g below room temperature, indicating a rubber-like amorphous structure. The presence of T_gs from PLAE and PLA indicates poor miscibility of the PTMEG and PLA components, which is consistent with the FTIR results. For the DSC curves in the first run, the T_gs of PLAE10–PLAE30 were not unambiguously determined, thus the second run was used to analyze the T_g of all blends.

It can be seen in Fig. 3b and Table 3 that all DSC curves for PLA/PLAE blends at different ratios have two obvious T_gs between 18–22 °C and 56–60 °C, resulting from PLAE and PLA.

This journal is © The Royal Society of Chemistry 2016

Published on 01 March 2016. Downloaded by UNIVERSITY OF CINCINNATI on 23/09/2016 02:17:08.

Table 3 Thermal test data of PLA, PLAE and the investigated PLA/PLAE blends

Samples	$T_{g\text{-PTMEG}}{}^{b}$ (°C)	$\Delta T_g{}^{c}$	$T_{g\text{-PLAE}}{}^{a}$ (°C)	$T_{g\text{-PLA}}{}^{a}$ (°C)	$T_{c\text{-PLAE}}{}^{b}$ (°C)	$T_{c\text{-PLA}}{}^{b}$ (°C)	$\Delta H_c{}^{b}$ (J g^{-1})	$T_{m\text{-PLAE}}{}^{b}$ (°C)	$T_{m\text{-PLA}}{}^{b}$ (°C)	$\Delta H_m{}^{b}$ (J g^{-1})	$X_c{}^{b}$ (%) (J g^{-1})
PLA	—	—	—	59.61	—	105.10	1.667	—	151.34	2.08	0.44
PLAE10	—	94.78	18.78	59.36	—	118.86	18.98	—	149.08	22.44	3.59
PLAE20	—	96.25	20.25	58.89	—	106.41	18.25	145.38	149.08	22.59	4.69
PLAE30	—	97.45	21.45	58.57	—	103.96	16.95	144.63	150.09	18.91	2.21
PLAE40	—	97.66	21.166	58.40	—	102.87	18.37	143.65	149.17	19.74	1.61
PLAE50	—	97.51	21.51	57.64	—	101.16	18.76	143.16	149.25	20.64	2.31
PLAE60	—	97.75	21.75	57.69	—	100.34	17.14	142.63	149.13	17.63	0.63
PLAE70	—	98.10	22.10	57.42	88.93	104.84	17.26	142.24	149.50	21.71	6.04
PLAE80	—	98.15	22.15	56.54	89.19	107.85	12.84	143.07	149.63	16.16	5.06
PLAE100	−39.75	98.26	22.26	—	88.15	—	12.01	141.41	—	15.55	6.05
PLAE80	—	98.25	21.82	57.61	90.49	—	10.40	142.47	—	15.87	5.84
PLAE	—	98.37	22.20	—	91.98	—	14.97	141.45	—	15.81	0.90

[a] The glass transition temperatures were determined from the second heating run. [b] The glass transition temperatures, melting point, crystallization temperature, heat of fusion and crystallinity data were determined from the first heating run. [c] ΔT_g was obtained from the difference between the T_g of blends due to soft segments ($T_{g\text{-PLAE}}$) and T_g of macrodiols (PTMEG, −76 °C).

In general, DSC is commonly used for discriminating between the miscible and immiscible polymer blends. While a single T_g is the indication of a miscible system, two T_gs is typically characteristic of an immiscible blend.

Soft and hard segment crystallization and phase separation can be estimated from thermal transitions such as glass transition temperature, melting temperature, and crystallization temperature.[37–39] Our results indicate the poor miscibility of PLA and PLAE. In general, with an increased PLAE content, the $T_{g\text{-PLAE}}$ tends to shift to a higher temperature while $T_{g\text{-PLA}}$ is slightly lowered. These findings indicate a phase separation in the blends at the microscopic level.

To investigate phase separation between the hard and soft segments, ΔT_g representing the difference between the T_g of blends due to soft segments ($T_{g\text{-PLAE}}$) and T_g of macrodiols (PTMEG, −76 °C) was calculated and listed in Table 3. Smaller ΔT_g reflects decreasing inter-phase interaction and solubilization. In other words, a well phase-separated system can be obtained for a small ΔT_g.[40,41] The results listed in Table 3 show that ΔT_g decreases with decreasing PLAE content in the blends. Consequently, large ΔT_gs demonstrate incomplete phase separation in the blends. However, even for these two non-immiscible components, we found slight shifts of their T_gs for the PLA- and PLAE-rich phases in the blends. We therefore conclude that there are interactions between PLAE and PLA at the molecular level (*e.g.*, hydrogen bonding). The phase separation is inversely associated with the PLAE content, resulting from the partial miscibility of the two components. On the other hand, for samples of PLAE70 and PLAE80, two separated crystallization peaks are observed, demonstrating two crystalline materials being formed at lower temperatures, that is related to the PLAE component. As can be seen in Fig. 3a, the low-temperature peaks gradually merge with the high-temperature ones. In contrast, PLAE50 and PLAE10 only display one crystallization peak in the DSC curves (Fig. 3a). As shown in Fig. 3c, the blends with PLAE content less than 40% exhibit lower crystallization peaks, while higher crystallization peaks are observed for the samples above 40% (Fig. 3a).

The reduction effect of PLAE on PLA crystallization was found at the high PLAE content. In contrast, low PLAE content in the blends promotes crystallinity of PLA. For the separated melting peaks, few reported the lamellar rearrangement during crystallization of PLA. The low-temperature peak appears on the melting endotherm of the original crystallites, while the high-temperature one is for the recrystallized material. The two melting peaks can be a result of the polymorphic crystalline transition of PLA.[42] For melting peaks of blends, the low-temperature peaks are up-shifted when decreasing the PLAE content and the high-temperature peaks remain in the same position for all blends. The two melting endotherm peaks appear less distinct in the second run and the low-temperature peaks become more pronounced. The less perfect PLA crystals with lower T_m are expected to grow with chain rearrangement of PLAE.

The formation of crystalline is expectedly affected by the soft PTMEG segments in PLAE, which is characterized by the low-temperature peaks. Provided less obstacles to the movements

Published on 01 March 2016. Downloaded by UNIVERSITY OF CINCINNATI on 23/09/2016 02:17:08.

of molecular chains in the crystalline phase, it leads to early crystalline collapse during the melting process.[43] Moreover, the T_c of the blends decreases with the increasing PLAE content, indicating the contribution of PTMEG segments to the formation of PLAE crystalline. The crystallinity of the blends is enhanced compared with that of plain PLA counterpart, as shown in Table 3. The increase of ΔH_m and ΔH_c was reported to be caused by the enhanced crystallinity resulting from the reduced urethane linkage content.[44] It is noted in the second run DSC curves (Fig. 3c) that no separated crystallization peaks and less distinct melting peaks are observed, suggesting less separated PLA- and PLAE-rich phases in the blends through self-adjustment of PLAE molecular chain.

3.3. DMA analysis

The dynamic mechanical analysis (DMA) results for the blends with various PLAE contents are presented in Fig. 4. The temperature dependence of the storage modulus E' for PLAE100, 2002D PLA, and their blends is shown in Fig. 4a. For PLAE, the storage modulus E' falls off gradually at −40 °C due to glass transition of the PTMEG segment. E' of PLAE80 also shows the same trend. E' continues to increase as PLAE content decreases. tan θ is a parameter associated with the glass transition of the amorphous phase of PLA. The maximum of respective tan θ peak (T'_g) is seen to decrease with increasing PLAE content. As expected, the T'_g values associated with the glass transition of PLA are in agreement with those found by DSC. In addition, when the PLAE content increases, tan θ becomes broadened and shifted to a lower temperature. In contrast, high and sharp peaks at higher temperatures are observed in 2002D and PLAE10. It indicates that blended system with a higher PLAE content is comparatively heterogeneous with gradually reduced restriction of segment motion. It is also noted that the $T_{g\text{-PTMEG}}$ and $T_{g\text{-PLAE}}$ observed in DSC are not found in the DMA test, attributable to the low PTMEG segment content in the blends.

3.4. Mechanical properties and blend morphology

The stress–strain curves of the PLA/PLAE blends with various PLAE contents are shown in Fig. 5. Each sample was characterized by tensile tests at room temperature. The dependence of elongation at break and tensile strength on PLAE content is shown in Fig. 5c. The stress–strain curve of PLAE suggests a typical thermoplastic elastomer with no yielding point. It has

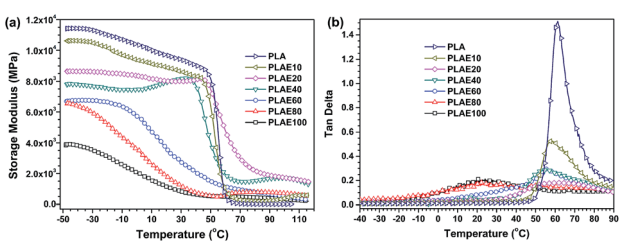

Fig. 4 DMA of pure PLA and blends with various multiple plasticizers content: (a) storage modulus and (b) tan δ.

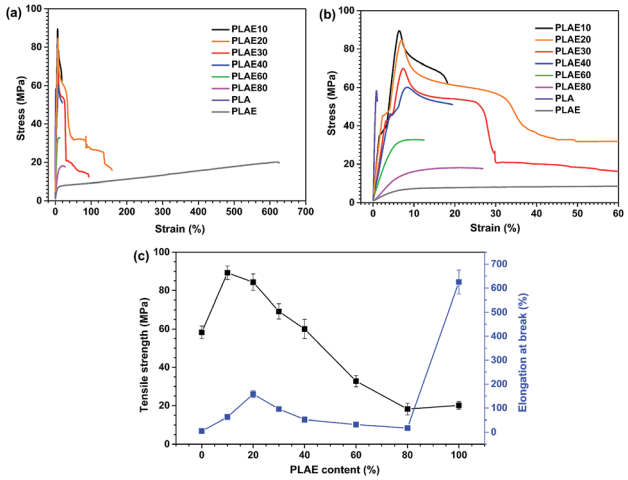

Fig. 5 (a) Representative stress–strain plot of each sample, (b) magnified image of stress–strain plot, 0–100% elongation (c) dependence of elongation at break and tensile strength on PLAE content. The error bars represent one standard deviation of the data, which is taken as the uncertainty of the measurement.

a high tensile strength of 20.1 MPa and excellent elongation at break (625.5%), exhibiting rubber-like elasticity. It shows noticeable strain hardening and its elastic strain keeps increasing within the strain range. We conclude that the PTMEG soft segment linked by urethane linkage enables stronger secondary bonding during extension, which is favorable for strain-induced crystallization. This is in accordance with the previously reported studies[45,46] that the strain-induced crystallization of the PTMEG soft segments is responsible for the upturn in stress–strain curves.

It should be noted that the extensibility is often governed by defects in the samples, and therefore, each experiment was repeated more than six times and the average test results were reported in order to ensure the reproducibility of the data. The stress–strain behavior of PLA varies drastically with the addition of PLAE as shown in Fig. 5a. No obvious yielding occurs for the plain PLA, which has high tensile strength but poor toughness. However, it is shown in Fig. 5b that for PLAE content above 50 wt%, no yielding point is observed, due to governing of the PLAE matrix in these blends. In contrast, for PLAE content below 50 wt%, an obvious yielding and necking is observed. The stress–strain curves of the blends exhibit an elastic deformation stress plateau even in the presence of 10 wt% PLAE. This clearly indicates the transition of PLA from brittle to ductile fracture. In addition, the tensile strength for mixtures from PLAE10 to PLAE30 is significantly higher than that of plain PLA. For PLAE10, the tensile strength even reaches 100.29 MPa and the elongation at break is significantly increased to 28.2% compared with 4.95% of plain PLA.

The tensile strength is gradually lowered with the PLAE content increases from PLAE10 to PLAE80. The elongation at break is also increased rapidly to 145% when PLAE increases from 10 wt% to 30 wt%, while the tensile strength is maintained at 70 MPa. These results indicate that PLAE effectively improves the toughness of the polymer blends with significant increase in

 This journal is © The Royal Society of Chemistry 2016

Published on 01 March 2016. Downloaded by UNIVERSITY OF CINCINNATI on 23/09/2016 02:17:08.

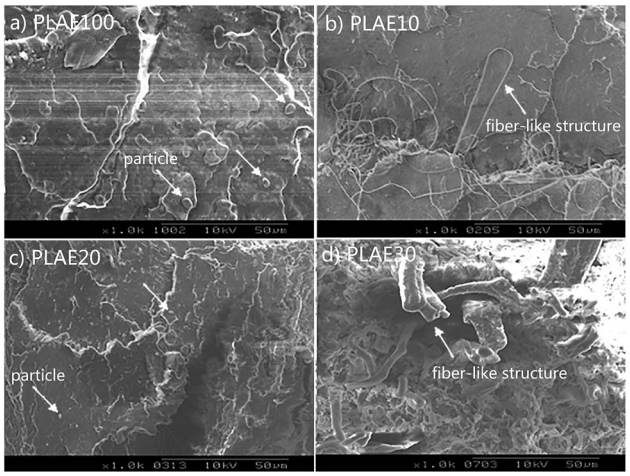

Fig. 6 SEM micrographs of tensile fractured surfaces of PLA/PLAE blends: (a) PLAE100; (b) PLAE10; (c) PLAE20; (d) PLAE30.

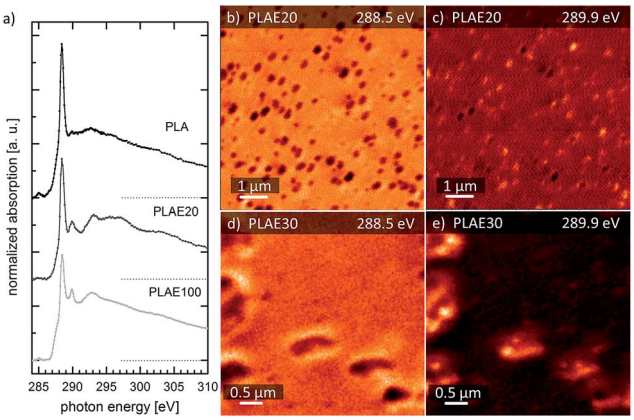

Fig. 7 (a) Comparison of the C1s NEXAFS spectra of PLA, PLAE20 and PLAE100 as derived from respective STXM image sequences. (b and c) STXM micrographs converted to OD (scan area: 8 × 8 μm^2) of a microtomed PLAE20 specimen recorded at the distinct NEXAFS resonances of PLA (b) or PLAE (c). (d and e) corresponding STXM micrographs for microtomed PLAE30 (scan area: 5 × 5 μm^2).

both tensile strength and elongation. With over 60 wt% PLA segment in PLAE, PLAE10 and PLAE30 each contains approximately 85 and 95 wt% PLA, respectively. Note that as the PLAE content is increased to above 40 wt%, its elongation drops to 22.0%, then gradually increases to 44.9%.

In order to understand the significantly improved mechanical properties of PLAE100 and the low-PLAE concentration blends (PLAE10 to PLAE30), SEM was employed to investigate the stretching fracture surfaces. As shown in Fig. 6a, stretching fracture surfaces of PLAE100 display a remarkably rough surface indicating ductile fracture during the mechanical test. It can also be seen that some spherical particles are uniformly dispersed in the continuous matrix, which is in good agreement with phase separation of PLAE100 as characterized by DSC and FTIR analysis. As shown in Fig. 6b, a fiber-like structure exists on the fracture surface which was not observed in our previous work.[21,47] The formation of the fiber-like structures plays an important role in the energy absorption during the tensile deformation. As a result, the tensile strength of PLAE10 reaches 100 MPa, and its elongation at break is significantly improved compared with plain PLA. For PLAE30, an extremely uneven surface is shown in Fig. 6d. These fibers exhibit larger diameters than those of PLAE10, indicating great deformation and rearrangement of the polymer chains during the test. However, in Fig. 6c the fracture specimen of PLAE20 demonstrates a rough surface similar to that of PLAE100. Some small spherical particles can be observed in the SEM image.

3.5. STXM and AFM observation and toughening mechanism of the PLA/PLAE blends

The results of the chemically sensitive STXM analysis are summarized in Fig. 7. Fig. 7a compares the integrated C K-edge NEXAFS spectra of the pure materials (PLA and PLAE100) with the spectrum of a microtomed PLAE20. All spectra are governed by a sharp resonance at 288.5 eV which is commonly attributed to the C1s → π* (C═O).[48] The resonance at 289.9 eV can be assigned to either C–H Rydberg states, or to a significant contribution of C–NH bonds for PLAE or in PLAE20.[49] According to literature, the spectral features in the range from 292 eV to 310 eV can be roughly sub-divided to *-resonances originating from carbon single bonds (292–300 eV) and carbon double bonds (300–310 eV). O K-edge NEXAFS spectra (not shown) have resonances at 532.4 eV and 535.5 eV that are unambiguously assigned to C═O and C–O–C bonds, respectively. Thus, the spectral features conclusively represent the molecular subunits, *i.e.*, C═O belongs to PLA, C–O–C to PTMEG, and C–NH to the HDI segment. These assignments are consistent with the spatial distribution and the phase separation of PLA, PTMEG, and HDI.

Fig. 7b and c depict the STXM micrographs of a microtomed specimen from PLAE20 recorded at two distinct resonances. The contrast reversal clearly indicates the distribution of two species and their phase separation at the nanometer level. The contribution of the PLAE domains agrees with its nominal concentration. Note that the signal-to-noise ratio in Fig. 7b is higher compared to that in Fig. 7c due to the maximum spectral contrast at 288.5 eV with respect to the minority C–NH species imaged at 289.9 eV.

Fig. 7d and e show the respective STXM micrographs from PLAE30 on an enlarged scale (compared to b and c). In the PLAE30 specimen, the image contrast shows more pronounced details compared to the low-concentration specimen. We also found fine structures of PLAE within the PLA matrix (diameter around 100 nm) as shown in Fig. 7e. The structural morphology of larger PLAE domains is different from PLAE20. The surroundings of PLAE inclusions (dark areas in Fig. 7d) indicate some variations in PLA density. Fig. 7e shows the C–NH resonance in the same area in which a finer structure is observed at higher image contrast. These finer structures are consistent with the results of the AFM images as shown in Fig. 8.

The tapping mode AFM was employed to investigate the phase structure of the microtomed specimens. For the respective specimens, the left images display the height and the ones on the right show the phase images, respectively. The scan

Published on 01 March 2016. Downloaded by UNIVERSITY OF CINCINNATI on 23/09/2016 02:17:08.

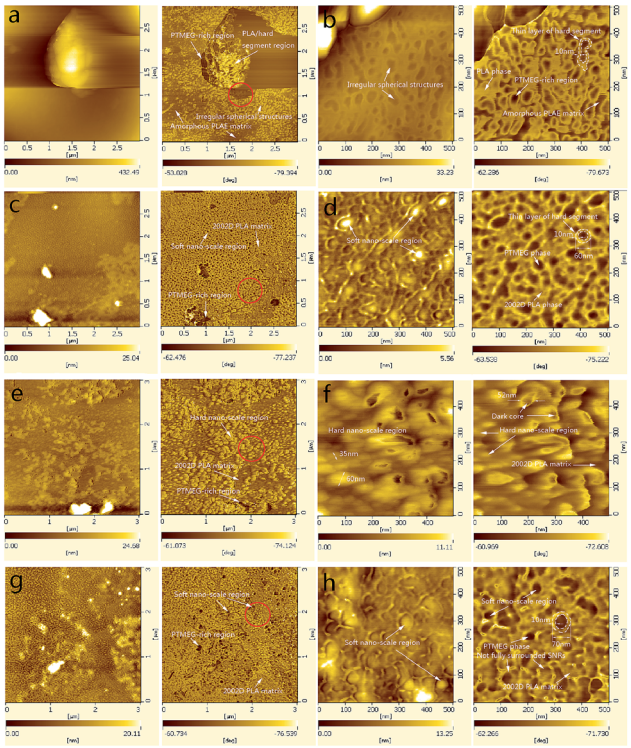

Fig. 8 Tapping mode AFM images (left column: topography, right column: phase image) of: (a) PLAE100 (scan range: 3 × 3 μm^2); (b) PLAE100 (500 × 500 nm^2), red cycle region; (c) PLAE10 (3 × 3 μm^2); (d) PLAE10 (500 × 500 nm^2), red cycle region; (e) PLAE20 (3 × 3 μm^2); (f) PLAE20 (500 × 500 nm^2), red cycle region; (g) PLAE30 (3 × 3 μm^2); (h) PLAE30 (500 × 500 nm^2), red cycle region.

ranges are 3 × 3 μm^2 or 500 × 500 nm^2. For pure PLAE the AFM image in Fig. 8a shows fine dispersion of irregular spherical structures with sizes within 100 nm in the matrix. In addition, the dark area observed in the phase image can be attributed to the PTMEG-rich region. It is also observed in the SEM image, as shown in Fig. 6, that the part with less contrast is the amorphous PLAE100 matrix (in agreement with DSC results indicating lower crystallinity for PLAE100 and PLAE10–30). The bright regions are likely the crystallized PLA and hard segments.[31,50] The hard segment region formed by hydrogen bonding[31] becomes irregular spherical structures as shown in Fig. 8b. These irregular spherical structures are dispersed in the amorphous PLAE100 matrix. It is observed that the thin layer of hard segment has a thickness around 10 nm. Aneja *et al.*[25] reported on the hard segment region approximately 6 ± 2 nm wide in polyurethane based on methylenediphenyl diisocyanate (MDI). They found, using AFM, that the width of hard segment was close to the results shown in Fig. 8b. They also found the lamellae shaped hard microphase separated from the soft PTMEG. The PTMEG and PLA phases observed in this study are consistent with the DSC results shown in Fig. 3a.

Fig. 8 shows the results of AFM study. As can be seen in this figure, the phase distribution is similar to that of PLAE10. The diameter of SNRs becomes larger (100 nm) than that of SNRs in PLAE10. The thin layer of the hard segment is observed around SNRs as shown in Fig. 8h. However, the phase separation decreases compared with PLAE10. The DSC results show that some SNRs are not fully surrounded by the hard segment. Some SNRs are collapsed due to chain orientation of 2002D PLA at the beginning of the stretching process. SNRs play a key role in absorption of energy at the nanoscale level. The fiber-like structure is formed from the elongated PTMEG segment. The effect of molecular chain changes effectively and improves the mechanical properties of PLAE30. As a result, 145% elongation at break and much higher tensile strength are achieved compared with plain 2002D PLA.

It is expected that the PLAE100 amorphous molecular chain is gradually oriented in the direction of stretching when subjected to tensile force. Consequently, the irregular spherical structures formed by hard segment collapse and the hard segment is oriented in the direction of stretching. The initial response to an imposed stress is stretching of the amorphous PLAE matrix chains. Efficient stress transfer to chains in hard segment domains causes them to breakup at flaws and rotate in the strain direction. It was reported that, further stretching of the PTMEG soft segment enabled stronger secondary bonding during extension, which was favorable for strain induced crystallization. The strain induced crystallization of the PTMEG soft segments is mainly responsible for the upturn in stress–strain curves.[46] The amorphous PLA segment undergoes strain induced crystallization, whereas the PLA-rich phase experiences only a small elongation. The orientation of the soft segment-rich phase with opposite alignment of the soft and PLA chains is also commonly observed in the hard segments of polyurethanes.[11,51–53]

In the case of PLAE10, the AFM images are different from that of PLAE100. As can be seen from Fig. 8c, a dark particle of PTMEG-rich region is observed. Moreover, the PTMEG-rich soft nano-scale region (SNR) is shown to have diameters around 30–80 nm, well dispersed in the 2002D PLA matrix. It can be seen from Fig. 8d that these SNRs are surrounded by a thin layer of bright region attributed to hard segment formed by hydrogen bonding. The SNR has a hard shell and soft core. This particular structure plays a key role in toughening PLAE10 during the tensile process.

2002D PLA chains outside SNRs are first oriented in the direction of stretching. These chains between SNRs then begin to orient, squeezing the SNRs in the PLAE10. The tensile force transfer through the hard segment "shell" creates a compression on the PTMEG segments in the SNRs, which absorbs energy at nano-scale and prevents deformation of the 2002D PLA chain. Furthermore, the PLA segment of PLAE improves the compatibility of molecule chains of PLAE and 2002D PLA by squeezing SNRs, which is consistent with the DSC results. Some PTMEG segments of the PTMEG-rich region in SNRs are oriented in the direction of stretching during the tensile process. These elongated PTMEG segments form fiber-like structure that improves the tensile strength and elongation at break at the same time, which is similar to the mechanism of fiber-reinforced composite.

The AFM images of PLAE20 are shown in Fig. 8e and f. The phase distribution appears different from those of PLAE100 and

 This journal is © The Royal Society of Chemistry 2016

Published on 01 March 2016. Downloaded by UNIVERSITY OF CINCINNATI on 23/09/2016 02:17:08.

PLAE10. It can be seen in this figure, the bright regions exhibit irregular particles of 100 nm that are well dispersed in the 2002D PLA matrix. In Fig. 8e and f, some particles have dark cores that are similar to the structure of SNR. These dark cores containing irregular particles, as shown in Fig. 8e and f, may not completely form SNRs. Most of the irregular particles without the dark core forms a "hard core-soft shell" structure. It was reported that the core–shell particles with a rigid core and a soft rubber shell were an effective toughener for semicrystalline polymers.[54] Upon orientation of the 2002D PLA chains, the assembly of the hard segment is gradually oriented in the stretching direction under the action of drawing and squeezing of the 2002D PLA chains. The oriented hard segment, separated from stretched irregular particles, acts as the stress-concentrator points at nano level and significantly improves the elongation of PLAE20.

4. Conclusions

In this study, PLA was blended with a thermoplastic polyurethane elastomer derived from PLA and PTMEG. The pure materials as well as the blends with different contents of PLA and PLAE were characterized in terms of mechanical properties, thermal behavior, and microstructure. The elongation at break of PLAE30 has reached above 140% while the tensile strength exhibits a high value of 70 MPa. An even higher tensile strength is achieved above 100 MPa for PLAE10 with significantly improved elongation at break compared with plain 2002D PLA. DSC shows partial phase separation in the PLAE and PLA/PLAE blends. Dynamic mechanical analysis indicates gradually reduced restriction of segment motion in the blended system with higher PLAE content. E' is found to increase with decreasing PLAE content in the blends. A soft nano-scale region was found in the matrix of PLA/PLAE blends with fine dispersion. A hard segment was observed by AFM in PLAE20. The irregular spherical structure was formed *via* hydrogen bonding in PLAE100 which can act as the stress concentrator points. In addition, a fiber-like structure was also found at the fractured surface of PLAE10 and PLAE30. These special structures are responsible for the significantly improved mechanical properties and play an important role in toughing and strengthening of the PLA-based thermoplastic elastomer and their blends. PLAE and PLA/PLAE will have high potential applications as biomedical implant materials, engineering plastics, and textile.

Acknowledgements

This work is supported by the National High Technology Research and Development Program of China (No. 2013AA032202), the National Natural Science Foundation of China (No. 51203118), the Fundamental Research Funds for the Central Universities, and the Open Funds for Characterization of Tongji University. STXM experiments were partly funded within the European Community's Seventh Framework Programme (FP7/2007-2013) under grant agreement No. 312284 (CALIPSO).

Notes and references

1 H. Liu, W. Song, F. Chen, L. Guo and J. Zhang, *Macromolecules*, 2011, **44**, 1513–1522.
2 S. Jacobsen and H. G. Fritz, *Polym. Eng. Sci.*, 1999, **39**, 1303–1310.
3 Z. Ren, L. Dong and Y. Yang, *J. Appl. Polym. Sci.*, 2006, **101**, 1583–1590.
4 Y. Lin, K. Y. Zhang, Z. M. Dong, L. S. Dong and Y. S. Li, *Macromolecules*, 2007, **40**, 6257–6267.
5 C. C. Chen, J. Y. Chueh, H. Tseng, H. M. Huang and S. Y. Lee, *Biomaterials*, 2003, **24**, 1167–1173.
6 Y. Hu, Y. S. Hu, V. Topolkaraev, A. Hiltner and E. Baer, *Polymer*, 2003, **44**, 5681–5689.
7 K. M. Nampoothiri, N. R. Nair and R. P. John, *Bioresour. Technol.*, 2010, **101**, 8493–8501.
8 L. Jiang, M. P. Wolcott and J. W. Zhang, *Biomacromolecules*, 2006, **7**, 199–207.
9 B. John and M. Furukawa, *Polym. Eng. Sci.*, 2009, **49**, 1970–1978.
10 E. A. Hasan, T. Cosgrove and A. N. Round, *Macromolecules*, 2008, **41**, 1393–1400.
11 K. Kojio, T. Fukumaru and M. Furukawa, *Macromolecules*, 2004, **37**, 3287–3291.
12 H. Yeganeh, M. Ghaffari and A. Jangi, *Polym. Adv. Technol.*, 2009, **20**, 466–472.
13 A. Nagatani, T. Endo, T. Hirotsu and M. Furukawa, *J. Appl. Polym. Sci.*, 2005, **95**, 144–148.
14 D. Cohn and A. F. Salomon, *Biomaterials*, 2005, **26**, 2297–2305.
15 A. Lendlein and S. Kelch, *Angew. Chem., Int. Ed.*, 2002, **41**, 2034–2057.
16 J. Ren, T. Yu, M. Yang, S. Gu and T. Ren, *Polym. Prepr.*, 2008, **49**, 466.
17 C. Zeng, N. W. Zhang, S. Q. Feng and J. Ren, *J. Therm. Anal. Calorim.*, 2013, **111**, 633–646.
18 C. Zeng, N. W. Zhang and J. Ren, *J. Appl. Polym. Sci.*, 2012, **125**, 2564–2576.
19 W. S. Wang, P. Ping, X. S. Chen and X. B. Jing, *Eur. Polym. J.*, 2006, **42**, 1240–1249.
20 T. Yu, J. Ren, S. Gu and M. Yang, *Polym. Adv. Technol.*, 2010, **21**, 183–188.
21 T. Yu, J. Ren, S. Y. Gu and M. Yang, *Polym. Int.*, 2009, **58**, 1058–1064.
22 J. Ren, T. Yu, H. Li, T. B. Ren and S. Yang, *Polym. Compos.*, 2008, **29**, 1145–1151.
23 N. W. Zhang, C. Zeng, L. Wang and J. Ren, *J. Polym. Environ.*, 2013, **21**, 286–292.
24 N. W. Zhang, Q. F. Wang, J. Ren and L. Wang, *J. Mater. Sci.*, 2009, **44**, 250–256.
25 A. Aneja and G. L. Wilkes, *Polymer*, 2003, **44**, 7221–7228.
26 G. Tzvetkov, A. Späth and R. H. Fink, *Radiat. Phys. Chem.*, 2014, **103**, 84–88.
27 A. Spath, S. Scho Ll, C. Riess, D. Schmidtel, G. Paradossi, J. R. Raabe, J. Hornegger and R. H. Fink, *Ultramicroscopy*, 2014, **144**, 19–25.

Published on 01 March 2016. Downloaded by UNIVERSITY OF CINCINNATI on 23/09/2016 02:17:08.

28 A. Späth, H. Minami, T. Suzuki and R. H. Fink, *RSC Adv.*, 2014, **4**, 3272–3277.
29 B. Rösner, A. Späth and R. H. Fink, *J. Cryst. Growth*, 2013, **380**, 34–38.
30 J. Raabe, G. Tzvetkov, U. Flechsig, M. Boge, A. Jaggi, B. Sarafimov, M. G. Vernooij, T. Huthwelker, H. Ade, D. Kilcoyne, T. Tyliszczak, R. H. Fink and C. Quitmann, *Rev. Sci. Instrum.*, 2008, **79**, 113704.
31 L. Rueda-Larraz, B. F. d'Arlas, A. Tercjak, A. Ribes, I. Mondragon and A. Eceiza, *Eur. Polym. J.*, 2009, **45**, 2096–2109.
32 P. Krol, *Prog. Mater. Sci.*, 2007, **52**, 915–1015.
33 S. Pongkitwitoon, R. Hernández, J. Weksler, A. Padsalgikar, T. Choi and J. Runt, *Polymer*, 2009, **50**, 6305–6311.
34 J. Liu, D. Z. Ma and Z. Li, *Eur. Polym. J.*, 2002, **38**, 661–665.
35 C.-P. Chen, S. A. Dai, H.-L. Chang, W.-C. Su, T.-M. Wu and R.-J. Jeng, *Polymer*, 2005, **46**, 11849–11857.
36 S. S. Liow, *eXPRESS Polym. Lett.*, 2011, **5**, 897–910.
37 N. Yoshie, A. Asaka and Y. Inoue, *Macromolecules*, 2004, **37**, 3770–3779.
38 Y. H. Na, Y. He, N. Asakawa, N. Yoshie and Y. Inoue, *Macromolecules*, 2002, **35**, 727–735.
39 Y. H. Na, Y. Arai, N. Asakawa, N. Yoshie and Y. Inoue, *Macromolecules*, 2001, **34**, 4834–4841.
40 K. Kojio, M. Furukawa, S. Motokucho, M. Shimada and M. Sakai, *Macromolecules*, 2009, **42**, 8322–8327.
41 H. Lü and S. Zheng, *Polymer*, 2003, **44**, 4689–4698.
42 A. J. Nijenhuis, E. Colstee, D. W. Grijpma and A. J. Pennings, *Polymer*, 1996, **37**, 5849–5857.
43 F. Rezgui, M. Swistek, J. M. Hiver, C. G'Sell and T. Sadoun, *Polymer*, 2005, **46**, 7370–7385.
44 J.-B. Zeng, Y.-D. Li, Q.-Y. Zhu, K.-K. Yang, X.-L. Wang and Y.-Z. Wang, *Polymer*, 2009, **50**, 1178–1186.
45 S. Gu, M. Yang, T. Yu, T. Ren and J. Ren, *Polym. Int.*, 2008, **57**, 982–986.
46 S. G. Kim and D. S. Lee, *Macromol. Res.*, 2002, **10**, 365–368.
47 Q. Zhong, J. Ren and Q. Wang, *Polym. Eng. Sci.*, 2011, **51**, 908–916.
48 H. Ade and A. P. Hitchcock, *Polymer*, 2008, **49**, 643–675.
49 O. Dhez, H. Ade and S. G. Urquhart, *J. Electron Spectrosc. Relat. Phenom.*, 2003, **128**, 85–96.
50 S. Essa, J. M. Rabanel and P. Hildgen, *Eur. J. Pharm. Biopharm.*, 2010, **75**, 96–106.
51 C. Vogel, E. Wessel and H. W. Siesler, *Macromolecules*, 2008, **41**, 2975–2977.
52 K. Kojio, S. Nakamura and M. Furukawa, *J. Polym. Sci., Part B: Polym. Phys.*, 2008, **46**, 2054–2063.
53 M. Furukawa, Y. Hamada and K. Kojio, *J. Polym. Sci., Part B: Polym. Phys.*, 2003, **41**, 2355–2364.
54 Z. Ke, D. Shi, J. Yin, R. K. Y. Li and Y. W. Mai, *Macromolecules*, 2008, **41**, 7264–7267.

This journal is © The Royal Society of Chemistry 2016